JOURNAL OF GEOPHYSICAL RESEARCH, VOL. 115, A05308, doi:10.1029/2009JA014894, 2010

Modeling of multiple effects of atmospheric tides on the ionosphere: An examination of possible coupling mechanisms responsible for the longitudinal structure of the equatorial ionosphere

S. L. England,[1] T. J. Immel,[1] J. D. Huba,[2] M. E. Hagan,[3] A. Maute,[3] and R. DeMajistre[4]

Received 10 September 2009; revised 2 December 2009; accepted 30 December 2009; published 25 May 2010.

[1] A number of recent studies have highlighted the observational evidence for a coupling between atmospheric tides in the thermosphere and the electron density structure of the ionosphere. The most commonly proposed mechanism to explain this is an electrodynamic coupling between tides at E region altitudes and ion drifts at F region altitudes. However, based on both the observational evidence from recent satellite missions such as those of the neutral winds associated with nonmigrating tides at F region altitudes, and considering the theoretical effects of atmospheric tides on the thermosphere and ionosphere, more than one coupling mechanism must be considered. We use Sami2 is Another Model of the Ionosphere to test a set of electrodynamic and chemical-dynamical coupling mechanisms that could explain the link between tides in the thermosphere and the low-latitude ionosphere. We investigate the possible role of the vertical drifts during the both the day and around sunset, perturbations to the thermospheric neutral density and thermospheric [O]/[N_2], and tidal winds at F region altitudes. These simulations give an estimate of the sensitivity of the nighttime ionosphere to each of these coupling mechanisms. We then compare the results of these sensitivity tests with the effects of atmospheric tides on different thermospheric parameters as simulated by a self-consistent model of the atmosphere-ionosphere-electrodynamic system (thermosphere-ionosphere-mesosphere-electrodynamics general circulation model). This comparison shows that in addition to the E region dynamo modulation, the potential coupling between tides and the ionosphere via changes in thermospheric [O]/[N_2], meridional winds at F region altitudes, and modification of the vertical drifts around sunset could play an important role and all require further study, both with models and new observations.

Citation: England, S. L., T. J. Immel, J. D. Huba, M. E. Hagan, A. Maute, and R. DeMajistre (2010), Modeling of multiple effects of atmospheric tides on the ionosphere: An examination of possible coupling mechanisms responsible for the longitudinal structure of the equatorial ionosphere, *J. Geophys. Res.*, *115*, A05308, doi:10.1029/2009JA014894.

1. Introduction

[2] The highest plasma densities in the geospace environment are found in the low-latitude F region of the ionosphere. The dominant ion species in this region is O^+. O^+ is primarily produced by photoionization of atomic O [see, e.g., *Schunk and Nagy*, 2000]. The ionization rate of O is highest at the subsolar point, which for equinox conditions is at the geographic equator at noon. The net production of O^+ is highly dependent upon the recombination rate of O^+ via collisions with molecular species (primarily N_2 and O_2 [e.g., *Schunk and Nagy*, 2000]). During the daytime, horizontal wind motions in the E region create currents [*Kato*, 1956, 1957] that produce polarization electric fields in regions of conductivity gradients. For the case of the equatorial region, these fields are eastward and produce a vertical uplift of the plasma around the magnetic equator known as the fountain effect [*Martyn*, 1947, 1953]. This vertical motion is further enhanced around sunset by strong vertical drifts [*Woodman*, 1970; *Farley et al.*, 1986]. This, along with the subsequent redistribution along the magnetic field lines, tends to move plasma away from the magnetic equator, decreasing the plasma density in this region. As the plasma redistributes along the magnetic field lines to higher latitudes [*Hanson and Moffett*, 1966] the plasma accumulates into two band located on either side of the magnetic equator [*Namba and*

---

[1] Space Sciences Laboratory, University of California, Berkeley, California, USA.

[2] Plasma Physics Division, Naval Research Laboratory, Washington, D. C., USA.

[3] High Altitude Observatory, National Center for Atmospheric Research, Boulder, Colorado, USA.

[4] Johns Hopkins University Applied Physics Laboratory, Laurel, Maryland, USA.

0148-0227/10/2009JA014894

Maeda, 1939; *Appleton*, 1946]. After sunset, the large-scale latitudinal, local time (LT) and longitudinal structure of the airglow associated with the O^+ distribution can be imaged from space [e.g., *Carruthers and Page*, 1976].

[3] A number of recent studies have shown that the F region equatorial plasma density varies with a wave number four longitudinal structure in a fixed LT frame during equinox and northern hemisphere summer. This was first identified in the airglow associated with O^+ at F region altitudes observed after sunset [e.g., *Sagawa et al.*, 2005; *Henderson et al.*, 2005; *Immel et al.*, 2006; *England et al.*, 2006b], and has subsequently been observed in numerous other measures of ion density in the equatorial region [e.g., *Lin et al.*, 2007; *Kil et al.*, 2007; *Scherliess et al.*, 2008; *Wan et al.*, 2008; *Pedatella et al.*, 2008]. This wave-like structure has been linked to the longitudinally dependent forcing produced by nonmigrating atmospheric tides [e.g., *Immel et al.*, 2006; *Kil et al.*, 2008; *Liu and Watanabe*, 2008; *Lühr et al.*, 2007; *England et al.*, 2009]. *Immel et al.* [2006] first proposed that this was caused by the horizontal winds associated with the diurnal eastward propagating wave number three tide (DE3) at the E region altitudes (as simulated by *Hagan and Forbes* [2002] and observed by *Oberheide and Forbes* [2008]) that modify the $\mathbf{E} \times \mathbf{B}$ drifts associated with the E region dynamo [*Hartman and Heelis*, 2007; *Kil et al.*, 2007] and the authors argued that the modification of these drifts affects the resultant postsunset F region plasma density. This mechanism has been modeled in both mechanistic models [*Jin et al.*, 2008] and self-consistent models of the ionosphere and thermosphere [*Hagan et al.*, 2007, 2009; *Häusler et al.*, 2010] and the effect of varying $\mathbf{E} \times \mathbf{B}$ drifts on the postsunset airglow associated with O^+ has been calculated by *England et al.* [2008].

[4] Atmospheric tides are also believed to affect the thermosphere in other ways than simply modifying the horizontal winds at E region altitudes. One well-known example is the vertical advection associated with the migrating diurnal tide that has been shown to modify [O] at equatorial latitudes and the associated postsunset green-line airglow in the equatorial region [*Roble and Shepherd*, 1997; *England et al.*, 2006a]. The potential for such additional effects of atmospheric tides to affect the wave number four longitudinal structure seen in the ionosphere has so far not been examined. Here we shall investigate different coupling mechanisms between atmospheric tides and the longitudinal structure of the ionosphere and focus on their potential impact on the postsunset airglow associated with F region $[O^+]$. Section 2 will describe the observations of the variation with longitude of the airglow. In section 3 we shall use the SAMI2 model [*Huba et al.*, 2000] to perform a series of sensitivity studies to investigate the susceptibility of the airglow to perturbations in different thermospheric parameters that may be associated with atmospheric tides, specifically changes in thermospheric density, $[O]/[N_2]$ and thermospheric winds at F region altitudes. As the SAMI2 model is a mechanistic model of the ionosphere that simulates the relevant ion transport and chemistry but does not self-consistently model the thermosphere, it is ideally suited to such sensitivity studies. For the purpose of this study, we shall consider a generalized diurnal tide rather than specifically simulating the DE3 because several tidal components have been shown to have a significant impact on the postsunset F region airglow [*England et al.*, 2009]. In section 4 we shall compare the results of these sensitivity studies with the thermospheric parameters from a self-consistent simulation of the ionosphere and neutral atmosphere (TIME-GCM [*Roble*, 1995, 1999; *Roble and Ridley*, 1994])that includes the impact of a whole spectrum of atmospheric waves. In the absence of many of the necessary observations needed to constrain the amplitude and phase of the waves or their effects at F region altitudes simulated by the thermosphere-ionosphere-mesosphere-electrodynamics general circulation model (TIME-GCM), it is not the intention of this study to perform a comprehensive diagnosis of each of the proposed coupling mechanisms within this self-consistent model, but rather to compare the TIME-GCM parameters to the SAMI2 sensitivity studies in order to determine which of these coupling mechanisms warrant further study both with models and observations.

2. TIMED-GUVI Observations

[5] The disk observations of the 135.6 nm airglow from TIMED-GUVI offer a useful data set to compare against the latitudinal slices of the ionosphere simulated by SAMI2 because of the simple viewing geometry (unlike, e.g., IMAGE-FUV), fine latitudinal resolution (unlike, e.g., COSMIC GPS radio occultation) and the optically thin 135.6 nm emissions are relatively easy to compare against the model output produced by SAMI2 [see, e.g., *England et al.*, 2008]. The observations from 2002 have been the focus of numerous previous studies cited in section 1 because the medium-high solar EUV flux during 2002 produced high postsunset $[O^+]$ and hence a high signal-to-noise ratio for the observations made at this time. It should, however, be noted that the amplitude of nonmigrating tides in the thermosphere are lower at solar maximum relative to solar minimum due to the increased tidal dissipation at solar maximum. Here we shall focus on the observations from close to vernal equinox (April 2002), when interhemispheric winds have been shown to play only a minor role [*Henderson et al.*, 2005] and hence the dominant processes controlling the $[O^+]$ airglow distribution are the daytime $[O^+]$ production rate, the equatorial fountain and any influence from symmetric neutral wind patterns associated with atmospheric tides in the thermosphere. Following *England et al.* [2008], we shall focus on observations from around 2100 LT (coming from days 86–95 of 2002), which is after the effects of the strong vertical drifts around sunset, away from any 135.6 nm dayglow but still early in the evening when the airglow is bright. Figure 1 shows the distribution of airglow brightness observed by TIMED-GUVI during his period. Also following *England et al.* [2008], we shall focus on the maximum in the emission brightness around 180°–210° longitude and the adjacent minimum in the emission brightness around 135°–165° longitude, which are indicated in Figure 1. This is the region in which the inclination and offset of the magnetic equator in the geographic reference frame is both small and similar for both of these locations, so the main difference between these two location comes from nonmigrating tides. As we are interested in the complete latitudinal profile of the airglow brightness and not simply the peak brightness, we shall not use the GUVI

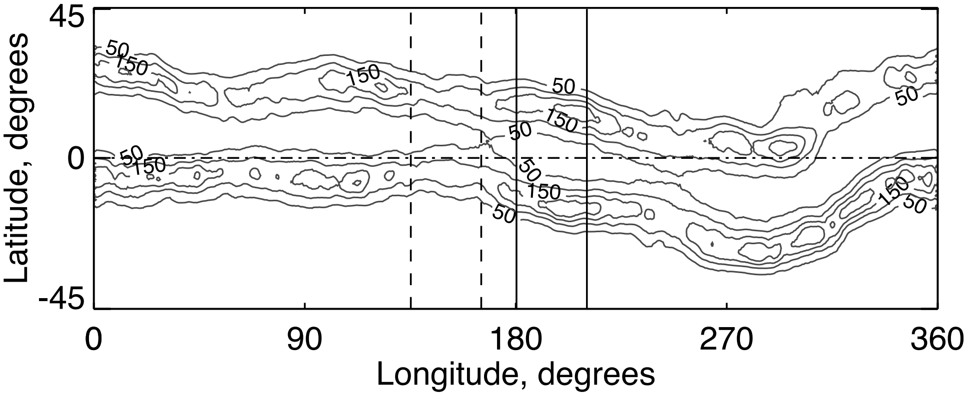

Figure 1. Plot of the 135.6 nm emission brightness in the nadir direction as a function of latitude and longitude at 2100 LT observed by TIMED-GUVI from days 86–95 of 2002. Contours are drawn at intervals of 50 Rayleighs. The dot-dashed horizontal line shows the geographic equator. The dashed vertical lines mark the region referred to in the text as the minimum brightness, and the solid vertical lines mark the region referred to as the maximum brightness.

analysis of *Henderson et al.* [2005] as presented by *England et al.* [2008], but shall instead show the emission brightness observed as a function of latitude. Averaging over 10 days and 30° longitude minimizes the impact of equatorial plasma bubbles on the reported airglow brightness, which removes the need to use an analysis similar to *Henderson et al.* [2005], although some difference in the results should be expected.

[6] Figure 3a shows the mean brightness of the 135.6 nm airglow observed by GUVI for these dates and local times. To simplify the comparison of data at the two different longitudes, the brightness has been plotted against latitude relative to the equatorial trough. The average of the brightness of the two anomaly peaks in the maximum brightness case is ~1.6 times as high as that for the two anomaly peaks in the minimum case. The peaks are also located a few degrees further poleward for the maximum case compared to the minimum. As noted by *England et al.* [2008], the absolute value of the brightness observed by GUVI during this time is less than that simulated by SAMI2, but it is the relative change in the airglow pattern between the two longitude sectors shown here that we shall use to test against the SAMI2 model output as it is the relative change in this parameter that represents the impact of atmospheric tides on the airglow, whereas the absolute value depends on a number of factors such as solar F10.7 flux that are not associated with atmospheric tides.

3. SAMI2 Model Simulations

[7] SAMI2 is a two-dimensional, first principles model of the low-latitude and midlatitude ionosphere [*Huba et al.*, 2000]. A full description and complete source code for the model is available at http://wwwppd.nrl.navy.mil/sami2-OSP/index.html. As the E × B drift and thermospheric inputs are not self-consistently calculated by the model, they can be changed arbitrarily and in isolation, which is essential for the present study. The model includes a detailed description of O^+ photochemistry and transport which allows it to realistically simulate the postsunset 135.6 emission brightness as described by *England et al.* [2008], using the numerical coefficients given by *Meléndez-Alvira et al.* [1999, and references therein] to calculate the line-of-sight-integrated airglow brightness. The following sections will detail the series of sensitivity studies performed with the SAMI2 model and the rationale for each.

3.1. SAMI2 Control Simulations

[8] The sensitivity studies presented in this section are aimed at determining what magnitude of each of the changes in the thermospheric and ionospheric inputs to the SAMI2 model associated with the various effects of nonmigrating tides is required to reproduce the difference in the airglow at the two longitudes shown in Figure 3a. The tidal perturbation of the eastward electric field in the E region has been shown to be of sufficient amplitude to reproduce this difference. For the solar maximum conditions at 190° longitude and using the *Scherliess and Fejer* [1999] vertical drift model, SAMI2 simulates the airglow brightness that corresponds to the maximum brightness case shown in Figure 3a. *England et al.* [2008] showed that by decreasing the drifts associated with the E region dynamo by ~40%, which corresponds to the change in the E region electric field strength inferred from the equatorial electrojet as a function of longitude observations from *England et al.* [2006c], the SAMI2 simulations reproduce the basic features of the change between the maximum and minimum brightness cases shown in Figure 3a. The different vertical E × B drifts used in these two simulations are shown as a function of local time in Figure 2. The simulated airglow brightness for these two cases are shown in Figure 3b (data are after *England et al.* [2008]). Again, these are plotted against latitude from the geomagnetic equatorial trough to allow an easy comparison with Figure 3a. The average of the two anomaly peaks for the maximum brightness case are ~1.5 times as high and both are located a few degrees further poleward of those for the minimum brightness case. This compares well with the relative difference in these brightnesses of a factor of 1.6 observed by GUVI. For the SAMI2 simulations, the brightness of both sets of airglow peaks is both higher and located 3°–4° further from the equatorial trough than that observed by GUVI. Both of these

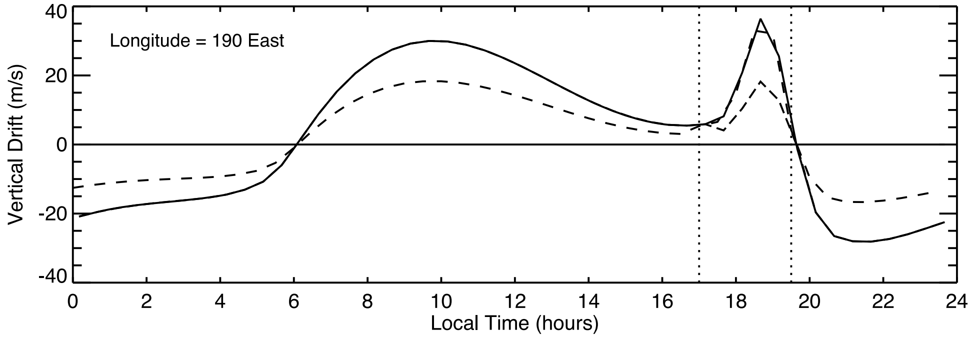

Figure 2. Plot of the vertical E × B drifts at the magnetic equator used in the SAMI2 model for the maximum (minimum) E × B drifts associated with the E region dynamo after *England et al.* [2008] shown by the solid (dashed) line and for the simulation of the change in E × B drifts around sunset shown by the dot-dashed line. The vertical dotted lines mark the boundaries of the local times over which the modified drifts area applied. All values are for 190° longitude.

effects are consistent with the **E** × **B** drift in the SAMI2 model being unrealistically high for these conditions. However, as the model does reproduce the relative change in the airglow peaks, *England et al.* [2008] argued that the change in the E region dynamo caused by the winds associated with nonmigrating tides in the lower thermosphere was sufficient in magnitude to account for the longitudinal structure of the postsunset equatorial airglow observed by GUVI. For the new sensitivity studies presented here, we shall attempt to find what magnitude of thermospheric or ionospheric driver is required in order to reproduce the airglow pattern for the perturbed case shown here in Figure 3b and therefore what other mechanisms could be of sufficient amplitude to either fully account for, or significantly contribute to the coupling between nonmigrating tides and the longitudinal structure in the F region ionosphere.

[9] Further comparison between the airglow patterns shown in Figures 3a and 3b reveals that the two airglow profiles from the SAMI2 simulations do not agree well with the observed brightness in the region of the equatorial trough. This difference may again be attributed to an overestimate of the vertical **E** × **B** drift used by the SAMI2 model during this time period. While it would in principle be possible to tune the vertical **E** × **B** drifts to provide the best reproduction possible for the observed airglow structure, this is not the goal of this work. Rather the goal of this study is to find the sensitivity of the airglow structure to various thermospheric and ionospheric drivers and compare these to the sensitivity of the airglow of changes in the E region dynamo fields. The SAMI2 simulations shown in Figure 3b provide an adequate reference point for such a sensitivity study.

3.2. SAMI2 Sensitivity Studies

[10] In this section we will describe the potential effects of atmospheric tides on a number of thermospheric and ionospheric parameters that could lead to changes in the F region nighttime O^+ density. Each individual section will then address the details of the experiment performed, and in section 5 we will compare the size of perturbation required with observed and/or modeled parameters to assess the feasibility of that perturbation as a major contributing factor in the coupling of atmospheric tides to the F region ionosphere.

3.2.1. Modification of the E × B Drifts Around Sunset

[11] The strong vertical drifts around sunset associated with the F region dynamo [*Rishbeth*, 1971; *Woodman*, 1970; *Farley et al.*, 1986] have a substantial impact on the height of the F region and separation of the two crests of the equatorial ionospheric anomaly (EIA) after sunset. This is especially true during times of high solar activity such as those present during 2002 when the GUVI observations shown in Figure 3a were made [*Fejer et al.*, 1991]. As the wave number four pattern has been seen in the daytime O^+ density structure [*Lin et al.*, 2007], the strong vertical drifts around sunset cannot be the sole cause of the longitudinal variation in the density of the F region ionosphere, but may still play a significant role in that structure seen after sunset. It is therefore worth considering how large a variation in the **E** × **B** drift during this LT period would be required to produce a longitudinal variation comparable to that shown from the E region dynamo fields in Figure 3b.

[12] Observations of the **E** × **B** drift close to sunset from ROCSAT-1 described by *Kil et al.* [2008] do not show a wave number four pattern, which suggests that if one exists, it is small in amplitude. However, *Liu and Watanabe* [2008] have observed that the wave number four pattern in the electron density at F region altitudes is more prominent after sunset than during the daytime, which they argued was the result of the drifts around sunset. They argued that longitudinal gradients in the conductivity close to the terminator that are created by the daytime longitudinal gradients in ion density could modify the strength of the **E** × **B** drifts at sunset [*Abdu et al.*, 2003].

[13] Here we perform simulations using the SAMI2 model and introduce a change in the strength of the **E** × **B** drifts around sunset by modifying the **E** × **B** drifts from the *Scherliess and Fejer* [1999] empirical model between 1700 and 1930 LT (shown in Figure 2). Figure 3c shows the control simulations where the daytime E region fields are changed (dashed line), along with the results from changing the sunset **E** × **B** drifts by reducing them by 50% (dotted line). This change is able to modify the peak brightness and location of that peak by approximately the same amount as the change to the E region dynamo fields. Changing the drifts around sunset also modifies the simulated brightness of the equatorial trough, which shall be discussed below.

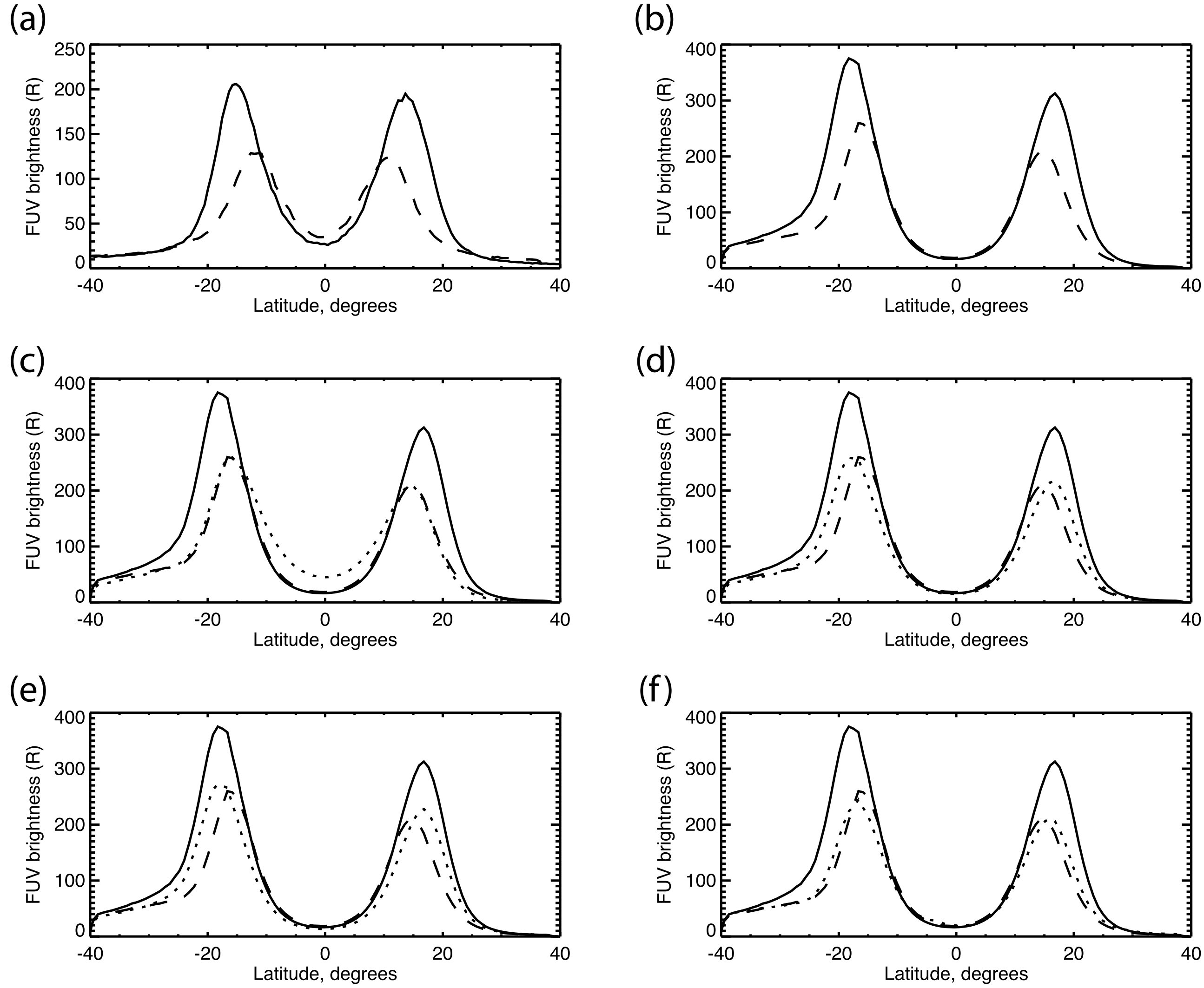

Figure 3. Plots of the 135.6 nm emission brightness in the nadir direction as a function of latitude relative to the equatorial trough at 2100 LT for the vernal equinox from (a) observations by TIMED-GUVI from days 86–95 of 2002 at (solid) a maximum in brightness (averaged over 180°–210° longitude) and (dashed) the adjacent minimum in brightness (averaged over 135°–165° longitude), (b) simulated with SAMI2 at 190° longitude for (solid) the maximum and (dashed) minimum E × B drifts associated with the E region dynamo after *England et al.* [2008], (c) as Figure 3b but including (dotted) the SAMI2 simulation of the change in E × B drifts around sunset, (d) as Figure 3b but including (dotted) the SAMI2 simulation of the change in thermospheric neutral density, (e) as Figure 3b but including (dotted) the SAMI2 simulation of the change in thermospheric O/N_2 ratio, and (f) as Figure 3b but including (dotted) the SAMI2 simulation of the change in thermospheric meridional winds.

3.2.2. Modification of the Thermospheric Neutral Density

[14] The perturbations of zonal winds caused by nonmigrating tides have been observed at F region altitudes by CHAMP [*Lühr et al.*, 2007; *Häusler et al.*, 2007]. *Hagan et al.* [2009] have shown that nonmigrating tides from the troposphere can propagate to F region altitudes in the TIME-GCM model. At these altitudes these tides can cause a longitudinal structure in the pressure, temperature, wind and density of the neutral atmosphere that exists in situ with the strong O^+ production and 135.6 nm airglow emissions. It is not clear how changes to the pressure or neutral temperature could significantly impact the postsunset airglow, but variations in the winds and density at these altitudes may provide alternative mechanisms for the coupling between nonmigrating tides and the F region ionosphere.

[15] The SAMI2 model uses the NRL-MSISE-00 model [*Picone et al.*, 2002] to provide inputs for the density and composition of the background atmosphere. To investigate the sensitivity of the postsunset airglow to perturbations in the neutral density that could come from atmospheric tides, we modify the total thermospheric density input to the SAMI2 model by multiplying the densities for each atmospheric species given by NRL-MSISE-00. In the absence of any observations to constrain the phase or altitude structure of such a modification of the neutral densities, we apply the

simplest perturbation that could be created by a nonmigrating diurnal tide. The densities of each atmospheric species are multiplied by a sinusoidal function with a period of 24 h that maximizes (decrease) at local noon and is applied to all altitudes. This perturbation takes the form of *density**(1 + A cos ($2\pi LT$(*seconds*)/86400)). Figure 3d shows the control simulations along with the results from SAMI2 when this sinusoidal function is applied with an amplitude of A = 0.4 (40%). This perturbation is able to modify the peak brightness of the postsunset airglow by the same amount as the change in the E region dynamo fields.

3.2.3. Modification of the Thermospheric [O]/[N_2] Ratio

[16] As described in section 1, the migrating diurnal tide has been shown to modify [O] in the mesopause and lower thermosphere at equatorial latitudes where the amplitude of this tide maximizes. This modification is the result of a vertical advection produced by this wave, in combination with strong vertical gradients in both the background [O] and the mean lifetime of O. At thermospheric altitudes, [O] has a strong impact on the O^+ production rate and molecular species such as N_2 have a strong impact on the O^+ recombination rate. The ratio of [O]/[N_2] is often used as a measure of the effect of the neutral atmosphere on the photochemical equilibrium of [O^+].

[17] As [O]/[N_2] in the thermosphere is strongly affected by large-scale vertical motions of the neutral atmosphere, such as those related to geomagnetic storms [*Burns et al.*, 1995], it is reasonable to assume that this ratio is also affected by nonmigrating tides at these altitudes. If this occurs at altitudes where the O^+ production rate is greatest and/or where the peak in the 135.6 nm airglow is strongest, it is reasonable to assume a change in [O]/[N_2] caused by nonmigrating tides could strongly affect the postsunset O^+ airglow brightness.

[18] Following the method used in the previous section, we apply a 24 h sinusoidal variation to the densities of [O] and [N_2] used as inputs to the SAMI2 model. As these two species vary out of phase with one another, we apply a perturbation that decreases [O] and increases [N_2] at local noon with respect to their background values given by NRL-MSISE-00. With such a simple perturbation, it is not possible to have the total neutral density unchanged at all locations and times, but we wish to minimize this variation in order to come as close to an idealized experiment as is possible with such a model and to distinguish this simulation as much as possible from that in the previous section. We therefore apply different amplitude perturbations to the [O] and [N_2]. Figure 3e shows the control simulations along with the results from SAMI2 when [O] is modified by a factor of 0.2 (20%) and [N_2] is modified by a factor of 0.1 (10%). This perturbation takes the form of *density**(1 + A cos ($2\pi LT$(*seconds*)/86400)) where A = 0.2 for [O] and A = −0.1 for [N_2]. At noon, this corresponds to a 25% change in [O]/[N_2]. This perturbation is sufficient to cause a change in the peak brightness of the airglow that is equivalent to that produced from modifying the E region dynamo fields.

3.2.4. Modification of the Thermospheric Meridional Winds

[19] The first symmetric mode of the DE3 is a Kelvin wave that has strong zonal winds and only very weak meridional winds associated with it. However, the magnetic field geometry of the equatorial ionosphere means that the ion density in this region and associated airglow is very sensitive to meridional winds at F region altitudes [e.g., *Thuillier et al.*, 2002]. Other nonmigrating tides have meridional wind perturbations associated with them that are larger than those of the first symmetric mode of the DE3 and therefore it is worth investigating the susceptibility of the postsunset 135.6 nm airglow to meridional winds at F region altitudes.

[20] The measurements from the CHAMP accelerometer have been used to quantify the zonal wind perturbations associated with nonmigrating tides at F region altitudes [*Lühr et al.*, 2007; *Häusler et al.*, 2007], but because of the polar orbit of the CHAMP satellite, these measurements are not able to provide observational constraints on the amplitude or phase of any longitudinal variations in the meridional winds at these altitudes. As the SAMI2 model is essentially a meridional model, the investigation of any zonal winds at ionospheric altitudes is not possible with this model. We shall therefore focus only on the effects of meridional winds at these altitudes.

[21] For this study, a diurnal variation similar to that in the previous sections is used, but here we introduce a sinusoidally varying wind that is added to the background meridional winds from the HWM-90 empirical model [*Hedin*, 1992]. In order to simulate a symmetric diurnal tidal mode, we introduce a meridional wind whose direction changes about the geographic equator (by convention, antisymmetric meridional winds correspond to a symmetric tidal mode) and for simplicity we vary the amplitude of that wind with a sinusoidal wave that maximizes such that the winds are poleward at local noon. This is applied equally to all altitudes. The winds are perturbed by a tidal wind of the form $\mp A$ cos ($2\pi LT$(*seconds*)/86400 + 7200/86400) (m s^{-1}), whose sign is negative for positive latitudes and vise versa and where A is the amplitude in m s^{-1}. Figure 3f shows the control simulations along with the results from SAMI2 when a diurnal wind is applied with amplitude of 20 m s^{-1}. This perturbation is sufficient to cause a change in the peak brightness and location of that peak that is equivalent to that produced by modifying the E region dynamo fields.

4. TIME-GCM Simulations

[22] In the absence of observational constraints on the parameters investigated in section 3 over the altitude range for which they are applied, we use a self-consistent simulation of the effects of nonmigrating tides on the thermosphere and ionosphere using the TIME-GCM model to provide a context in which to interpret the results of the sensitivity studies presented in section 3. The impact of atmospheric waves on the wave number four longitudinal structure of each key parameter simulated by TIME-GCM will be described in this section.

[23] The TIME-GCM is a three-dimensional time-dependent first principal model that calculates the dynamics, electrodynamics, photoionization, neutral gas heating, and the compositional structure of the middle and upper atmosphere. A more complete description of the model, which was developed at the National Center for Atmospheric Research, is given by *Roble* [1995, 1999] and *Roble and*

Ridley [1994, and references therein]. TIME-GCM is able to inherently calculate the atmospheric tides that are excited by the absorption of ultraviolet and extreme ultraviolet radiation in the middle and upper atmosphere. Nevertheless, it cannot account for tidal components that are excited by latent heat release in deep tropical clouds or by the absorption of infrared radiation [*Hagan et al.*, 2007]. In order to get the tides of tropospheric origin into the TIME-GCM, the lower boundary (i.e., 10 mb; ~30 km) of the model is disturbed with results of the global scale wave model (GSWM) which can account for the missing tides [e.g., *Hagan and Forbes*, 2002, 2003].

[24] For the March simulation discussed herein and on which *Häusler et al.* [2010] reported, we ran the TIME-GCM with 2.5° by 2.5° horizontal resolution and 4 grid points per scale height in the vertical. We ran the model to get a diurnally reproducible state with constant 10.7 cm solar radio flux (F10.7) value of 75, the hemispheric power value [after *Evans*, 1987] of 8 GW, and the cross-cap potential drop of 30 kV. While the input F10.7 value does not match that measured during the vernal equinox of 2002 (~170), the nonmigrating tides simulated by the TIME-GCM at F region altitudes for this model run have been compared in detail with the observations from the CHAMP satellite [*Häusler et al.*, 2010] that correspond to an F10.7 value of ~128. This means that the calculated values of the nonmigrating tides from this simulation can be interpreted within some observational constraints. In addition, it is worth noting here that while some differences in the wave number four pattern have been noted between solar minimum and solar maximum [*Liu and Watanabe*, 2008], these changes are small compared to the longitudinal structure that we are investigating here.

[25] *Häusler et al.* [2010] have presented the results from the TIME-GCM simulation for March, along with the CHAMP data for the same season. They showed that there is a strong wave number four variation in the thermosphere simulated by the model near its upper boundary (~400 km altitude). This wave number four variation comes from the combination of three waves in the model. These are DE3 tide, the semidiurnal eastward propagating wave number two tide (SE2) and a stationary planetary wave with zonal wave number four (sPW4). The CHAMP observations also reveal the presence of a semidiurnal westward propagating wave number six tide (SW6) that also creates a wave number four pattern in a constant local time reference frame, but which is essentially absent in the TIME-GCM simulations. This picture of a superposition of several waves, each with the same horizontal wavelength but different vertical structures and frequencies, is substantially more complex than that considered in section 3. *Immel et al.* [2009] have shown that a planetary wave can affect the wave number four variation in the postsunset airglow structure, although the authors did not determine the mechanism by which this occurred.

[26] In this section we shall analyze the TIME-GCM model parameters to investigate the effects of each of these three temporal components and also their combined effects at local noon, which is the most significant local time for the production of O^+ observed in the airglow at ~2100 LT [*England et al.*, 2008]. From the TIME-GCM, it is possible to extract the perturbations to the zonal and meridional winds, neutral mass density and $[O]/[N_2]$ associated with each wave as well as the vertical ion drifts at the magnetic equator resulting from the combined E and F region dynamos. Each of these can be determined over the range of latitudes and heights that is most relevant to our sensitivity studies presented in section 3.

[27] The latitudes at which the equatorial airglow arcs are located are the most significant for considering the effects of any meridional wind perturbations. Here we will examine the winds from 0° to 30° latitude (as the winds are divergent/convergent about the geographic equator, this latitude range is more appropriate than −30°–30°). For all other parameters, we shall consider the range −30°–30° latitude, where the O^+ production rates and 135.6 nm airglow are greatest. The values of each of the parameters studied in section 3 are shown in Figure 4 as a function of longitude and height for local noon. The mean value at each height (which includes the zonal mean and all migrating tidal components) has been removed so that the variations with longitude can be clearly seen at all altitudes. The three wave components that make up this resultant pattern are shown as a function of altitude in Figure 5. Figure 6 shows the vertical plasma drift at the magnetic equator as a function of local time and longitude near the upper boundary of the model ~400 km altitude. This can be compared with the vertical drifts measured by ROCSAT-1 at the magnetic equator at ~600 km altitude presented by *Kil et al.* [2008].

5. Discussion

[28] Before discussing the TIME-GCM model output and the SAMI2 sensitivity studies, it is worth comparing the zonal wind and daytime **E** × **B** drifts from the TIME-GCM simulation with those observed at the F region altitudes. *Häusler et al.* [2010] has shown that, compared to the CHAMP zonal wind observations for March at ~400 km altitude, the TIME-GCM simulates too large an amplitude for the DE3 and SE2 tides by a few m s^{-1} each. The TIME-GCM calculates a noontime **E** × **B** drift at ~400 km altitude at the magnetic equator with a clear wave number four pattern in local time and varies in magnitude from 10 to 21 m s^{-1}. The drifts at the longitudes corresponding to the maximum and minimum airglow regions simulated in section 3 (180°–210° and 135°–165° geographic longitude, respectively) are 21 and 11 m s^{-1}, respectively, at local noon and 19 and 9 m s^{-1} averaged over 1000–1100 LT (corresponding to the ROCSAT-1 observations from *Kil et al.* [2007]). This represents a smaller average drift and larger variation with longitude than that observed by ROCSAT-1 that *Kil et al.* [2007] showed to be 28 and 24 m s^{-1} averaged over 1000–1100 LT (a summary of these drift velocities is given in Table 1). The drifts used in the SAMI2 simulations were 23 and 14 m s^{-1} at local noon and 28 and 17 m s^{-1} averaged over 1000–1100 LT. Again, these are significantly higher than those calculated by TIME-GCM, but the variation with longitude is comparable to (although still smaller than) the TIME-GCM drifts. The variation with longitude used in the SAMI2 simulations are based on the E region electric fields inferred from magnetometer measurements of the equatorial electrojet made by CHAMP, SAC-C and Ørsted. Both the CHAMP and TIME-GCM values come from ~400 km, whereas the ROCSAT-1

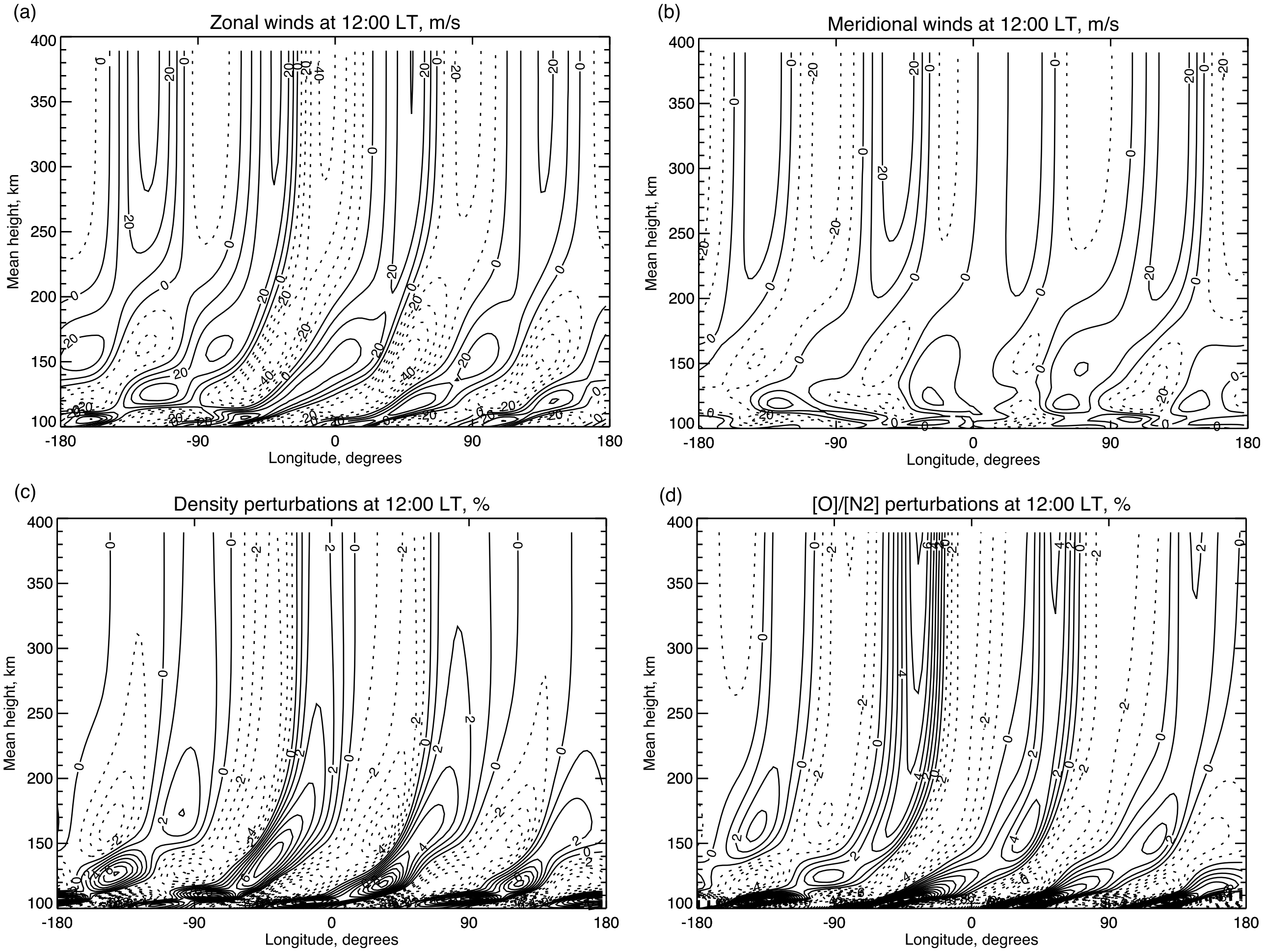

Figure 4. Longitude-height plot of (a) zonal winds averaged over <30° latitude (eastward positive), (b) meridional winds averaged over 0°–30° latitude (northward positive), (c) neutral density perturbations averaged over <30° latitude, and (d) perturbations to the thermospheric O/N_2 ratio averaged over <30° latitude at 1200 local time simulated by the TIME-GCM for March, low solar activity conditions (F10.7 = 75). The mean value at each height has been removed to more clearly show the perturbations as a function of longitude for all altitudes.

observations come from ~600 km. It is not clear if this difference could account for the differences in the strength of the longitudinal variation observed. It is also not clear why the average drifts calculated by the TIME-GCM are consistently smaller than those from ROCSAT-1 or from the *Scherliess and Fejer* [1999] empirical model used by SAMI2. The TIME-GCM simulation is for close to solar minimum conditions, whereas the observations and SAMI2 simulations are for moderate to high solar activity conditions, but the vertical drifts at local noon are not strongly affected by solar activity [*Fejer et al.*, 1991]. Given these unaccounted discrepancies between the TIME-GCM and the few observed and empirical parameters discussed here, it is not our intention to use the TIME-GCM as a definitive representation of the atmosphere, but rather the best available context in which to consider the SAMI2 sensitivity studies in the absence of the necessary observational constraints.

[29] For the case of the meridional wind perturbations, a diurnally varying meridional wind with amplitude of 20 m s^{-1} at F region altitudes is sufficient to create the change in the airglow observed after sunset. The wave number four pattern in the meridional winds calculated by TIME-GCM is substantially more complex than the perturbation used in the SAMI2 sensitivity study and is made up of three different waves each with the same horizontal wavelength but different periods, phases and vertical structures (see Figure 5b). Considering the combination of these at local noon, there is a rapid change in the meridional winds with altitude in the lower thermosphere, but essentially constant amplitude and phase across all heights above ~200 km. Therefore, the meridional winds will move the plasma in the same direction throughout the entire region of strong 135.6 nm airglow emissions. The total wave number four wind pattern at local noon at F region altitudes (Figure 4b) shows a variation in longitude of ±20 m s^{-1} between the two regions simulated in section 3. This is comparable in magnitude to the 20 m s^{-1} amplitude variation used in the SAMI2 simulation and thus warrants further investigation.

[30] The amplitude of the three wave components are shown in Figure 5b. The SE2 has the largest amplitude at F region altitudes, although both the DE3 and sPW4 also have significant amplitudes. The SE2 is believed to be less

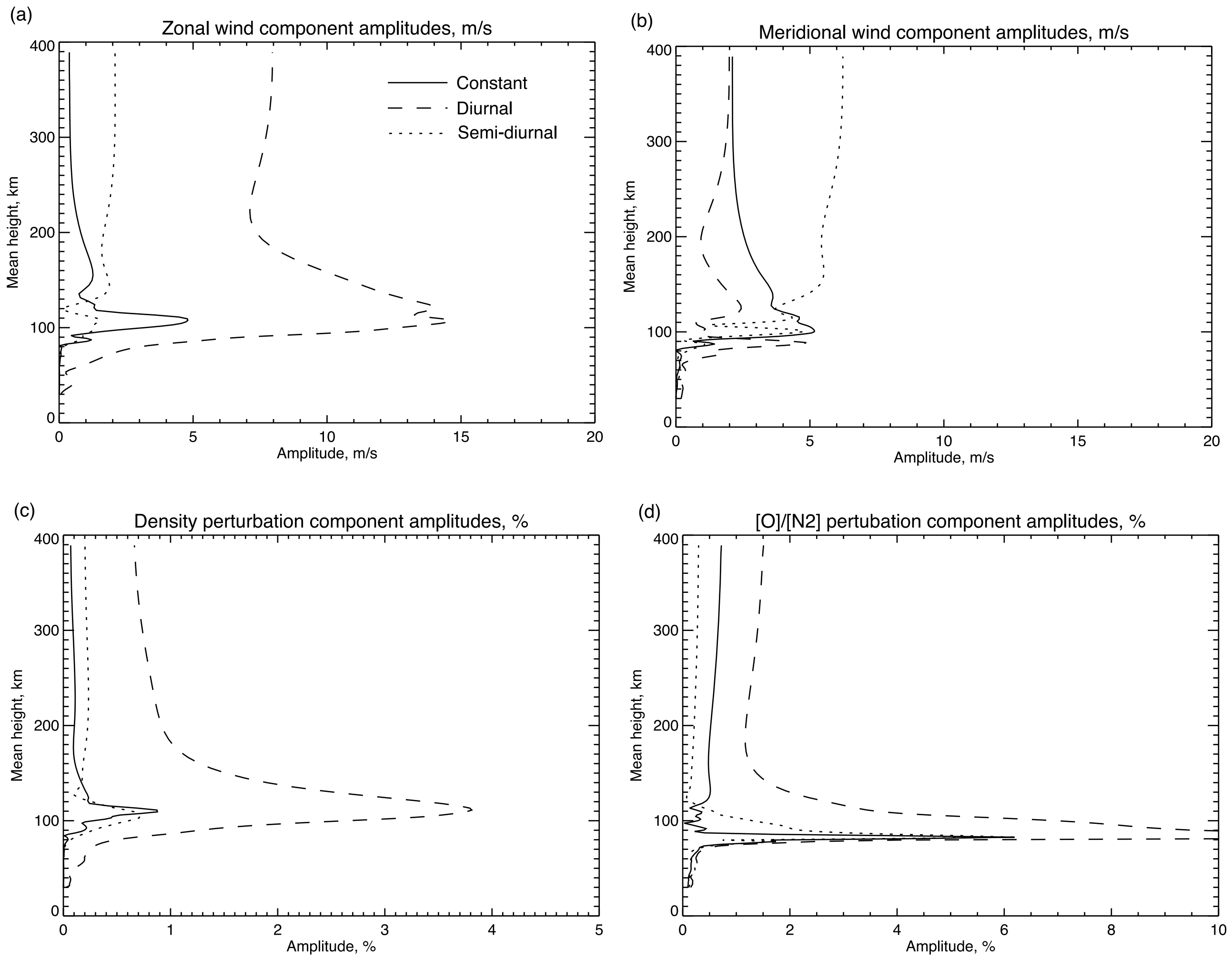

Figure 5. Height profiles of the amplitude of the (solid) constant, (dashed) diurnal, and (dotted) semi-diurnal components of the wave number four perturbation of each of the quantities from the TIME-GCM simulations shown in Figure 2, each averaged over the same latitudinal ranges as in Figure 2.

efficient at creating dynamo electric fields than the DE3 [*Forbes et al.*, 2008], so this wave should play less of a role in generating the perturbations to the E region dynamo fields, but could play a significant role at F region altitudes. The efficiency of this wave at producing a perturbation to the postsunset airglow structure requires a simultaneous consideration of the phase of the SE2, changes in the O^+ layer height and O^+ recombination rate which would require further study with a model such as SAMI2 that is beyond the scope of the present work. However, it is clear that the meridional winds at F region altitudes associated with non-migrating tides and planetary waves may play an important role in contributing to the wave number four pattern in the airglow observed after sunset and as such deserve further study.

[31] While the SAMI2 model does not allow us to estimate the effects of the vertical winds associated with non-migrating tides on the ionosphere, it is worth briefly discussing these here. Such winds can in principle affect the ionosphere in two ways: direct advection of O^+ plasma and modification of the neutral atmosphere. As with the meridional winds, the TIMED-GCM simulations suggest that the vertical winds associated with the SE2 dominate over the DE3 and sPW4, having amplitudes of 1 m s^{-1}, 40 cm s^{-1} and 4 cm s^{-1}, respectively, at 350 km altitude. Given that the pressure scale height is ~40 km and the O^+ scale height is ~100 km at this altitude, the direct effect of these vertical winds on the density of the atmosphere or ionosphere is not expected to be significant. Indeed, such potential impacts on the O^+ plasma are expected to be overwhelmed by the impact of the meridional wind, which is an order of magnitude larger (for this reason, any dynamo effects of these winds can presumably also be ignored). At lower altitudes, the vertical winds are significantly smaller, but may impact the ionosphere by altering thermospheric composition, e.g., $[O]/[N_2]$. Such effects on $[O]/[N_2]$ and subsequently on the ionosphere are discussed below.

[32] For the case of the neutral density perturbations, a diurnally varying perturbation of amplitude 40% is sufficient to create the change in the brightness of the peak airglow observed after sunset, but as shown in Figure 3d, is not able to reproduce the observed change in the latitude of that peak. The TIME-GCM simulations for both local noon and the three individual wave components show that the

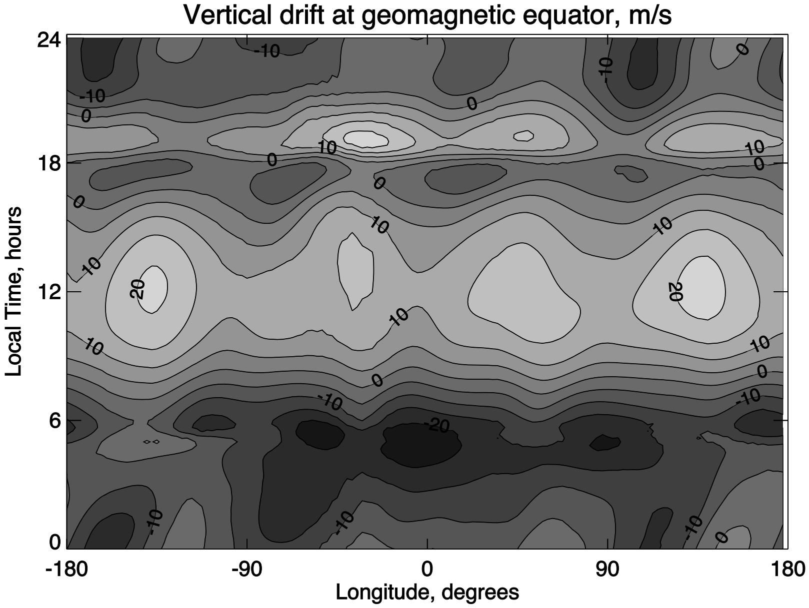

Figure 6. Longitude local time plot of the vertical drifts at the magnetic equator at 400 km altitude from the TIME-GCM simulations for March, low solar activity conditions. Upward is positive.

calculated neutral density perturbations do not exceed ~2–3% amplitude at F region altitudes. As this is far less than the 40% amplitude perturbation suggested from the SAMI2 sensitivity study, it is reasonable to conclude that perturbations to the neutral density associated with nonmigrating tides and planetary waves do not significantly contribute to the wave number four pattern in the postsunset airglow brightness.

[33] For the case of the changes in [O]/[N_2], a diurnal variation that corresponded to a 25% decrease at local noon is sufficient to create the change in the brightness of the peak airglow observed after sunset, but again this is not able to reproduce the change in latitude of that peak that has been observed. Figure 4d shows the change in this ratio at local noon as a function of both longitude and height. This shows both a strong wave number four and a wave number one variation as a function of longitude. In the longitude region that corresponds to the SAMI2 simulations, only a very small perturbation in [O]/[N_2] is calculated by the TIME-GCM, but around −45°–45° longitude these perturbations reach −3%–6% at local noon, which would correspond to a change of 9% compared to the 25% used in the SAMI2 sensitivity study. As both the amplitude of the changes in [O]/[N_2] is less than the 25% change from the SAMI2 sensitivity study and the change in [O]/[N_2] has been shown to be incapable of altering the latitude of the peak airglow brightness that has been observed by TIMED-GUVI and IMAGE-FUV, this mechanism cannot be the sole mechanism by which atmospheric tides couple to the F region ionosphere. However, a change of up to 9% does represent a significant fraction of the 25% from the SAMI2 sensitivity study and as such is worth considering as a potentially significant contributor to the wave number four pattern in the airglow observed after sunset.

[34] For the case of changes in [O]/[N_2] that are nonlinearly dependent upon the background vertical gradients in [O] and [N_2] and [O] reaction rates, it is not clear that the three components shown in Figure 5d are truly representative of the effects of each of the three wave components identified in the wind and density perturbations and as such cannot be discussed in any further detail.

[35] For the case of the changes to the vertical ion drifts around sunset, a perturbation of 50% is sufficient to account for both the change in the peak airglow brightness and location of that peak as observed by TIMED-GUVI. The vertical drifts around sunset calculated from TIME-GCM shown in Figure 6 reveal the strong vertical drifts in the model peak around 1900 LT, which is close to and just slightly later than those used in SAMI2 that peak around 1830 LT. The drifts calculated by TIME-GCM vary from ~2–22 m s^{-1} at this time and at the longitudes that correspond to the SAMI2 sensitivity study have values for 9 and 3 m s^{-1}. As with the drifts during the daytime, the vertical ion drifts calculated by TIME-GCM are significantly less than those used by SAMI2 or measured by ROCSAT-1 (see Table 1). As the drifts around sunset have been shown to vary greatly with solar activity [*Fejer et al.*, 1991], this difference may be explained by the difference in solar conditions between those used for the TIME-GCM simulations (F10.7 = 75) and those used in both the SAMI2 (F10.7 = 170) and those that correspond to the observations

Table 1. Values of Vertical Ion Drifts at the Geomagnetic Equator Either Observed by ROCSAT-1, Simulated by TIME-GCM, or Used in SAMI2[a]

Local Time (h)	Source	Drift Velocities (m s^{-1})
1200 LT	TIME-GCM	21, 11
1200 LT	SAMI2	23, 14
1000–1100 LT	TIME-GCM	19, 9
1000–1100 LT	SAMI2	28, 17
1000–1100 LT	ROCSAT-1	28, 24

[a] Values are given at the maximum and minimum locations as indicated in the text.

reported by *Kil et al.* [2007] (for mid to high solar F10.7 conditions).

[36] There is an apparent wave number four variation in the vertical drifts at sunset which is approximately in-phase with the wave number four variation in the daytime. The relative variation in these drifts calculated by TIME-GCM is greater than that used in the SAMI2 sensitivity study. As with the *Scherliess and Fejer* [1999] empirical model drifts used in the SAMI2 control case, the drifts calculated by TIME-GCM for around sunset are comparable in amplitude to those around midday, so it seems plausible that these are a significant contributor to the wave number four pattern in the postsunset airglow emissions that would exist if the atmosphere behaves as described by the TIME-GCM.

[37] The previous works that have considered the effect of the vertical ion drifts at sunset on the wave number four structure of the equatorial ionosphere do not offer a clear view of their potential effects. As discussed by *Liu and Watanabe* [2008], *Abdu et al.* [2003], and *England et al.* [2006b], the wave number four variation in the daytime ionospheric densities (and hence differences in the conductivities across the terminator that are responsible for the prereversal enhancement) could be expected to produce a wave number four variation in the drifts around sunset. Additionally, nonmigrating tides and planetary waves at F region altitudes can also be expected to produce a wave number four variation in the drifts around sunset. *Jin et al.* [2008] used an electrodynamics model of the ionosphere to simulate the effects of the DE3 tide on **E** × **B** at the magnetic equator. Their model produced a wave number four variation in the sunset drifts that was out of phase with that produced during the day. The vertical drifts from ROCSAT-1 from 1800 to 1900 LT reported by *Kil et al.* [2008] do not show any observational evidence of such a variation. As both the magnitude and LT of the strong upward drifts around sunset have been seen to vary greatly, it is possible that the averaging of the data used by *Kil et al.* [2008] was not appropriate for examining the wave number four structure in these drifts, or that such a variation does not exist at ~600 km altitude. The apparent intensification of the wave number four pattern in the electron density reported by *Liu and Watanabe* [2008] suggests that such a variation may be present in the ionosphere and has yet to be directly identified in the observations. Given the apparent strength of the wave number four variation in the drifts that is suggested by the TIME-GCM and electrodynamics model of *Jin et al.* [2008], the drifts at this time should be further investigated as a potentially large contributor to the wave number four pattern observed in the airglow after sunset.

[38] Examining Figure 3c in more detail reveals that the simulated brightness of the airglow in the equatorial trough is different for the SAMI2 simulation in which only the drifts around sunset are modified, compared with the change to the daytime drifts shown in Figure 3b. The value of the simulated airglow brightness is ~50R at the equatorial trough for the case of the modified drifts around sunset. The increase in the airglow brightness in this region is the result of a weakening of the equatorial fountain effect after sunset in this case, and a corresponding reduction in the transport of O^+ from the equator to higher latitudes. Such an effect is not seen in the SAMI2 model results when only the daytime **E** × **B** drifts are reduced as in Figure 3b. The value of the airglow brightness simulated at the equatorial trough shown in Figure 3d is comparable to that observed by TIMED-GUVI shown in Figure 3a, which suggests that the **E** × **B** drifts around sunset used by the SAMI2 model are too high in the control case. Further examination of the two longitude sectors shown in Figure 3a reveals that the brightness of the airglow trough observed by GUVI is slightly higher for the case when the maximum airglow brightness is lower. This is consistent with a slight weakening of the **E** × **B** drifts around sunset in the minimum brightness case, albeit less than that simulated here.

6. Conclusions and Future Work

[39] 1. Nonmigrating atmospheric tides have a number of impacts on the thermosphere at both E and F region altitudes.

[40] 2. Using the mechanistic SAMI2 ionospheric model, we have shown that the kinds of impacts atmospheric tides may have on thermospheric density, meridional winds at F region altitudes and composition ($[O]/[N_2]$) can reproduce some or all of the longitudinal structure seen in the postsunset airglow associated with O^+ recombination. Further, we have shown that the modification of the **E** × **B** drifts associated with both the E and F region dynamos through modification of the conductivities and/or neutral winds at E and F region altitudes are able to reproduce the longitudinal variation of this airglow.

[41] 3. Through a comparison of the sensitivity of the airglow to each of the modifications listed above with a self-consistent calculation of the impact of nonmigrating tides and planetary waves on the thermosphere and ionosphere using the TIME-GCM, we have shown that the influence of these waves on the longitudinal structure of the postsunset airglow may occur via electrodynamics (changes to the E region dynamo fields or the F region dynamo fields) or advection by in situ meridional neutral winds, with a potentially significant contribution also coming from changes to the O^+ production and loss rates via changes to the neutral composition ($[O]/[N_2]$). We have shown that tidal perturbations to the thermospheric density have a negligible impact on the postsunset airglow.

[42] 4. It is clear that the wave number four longitudinal variation of $[O^+]$ simulated by the TIME-GCM model is the result of some combination of the effects listed above, and not purely the result of changes to the E region dynamo fields as has been previously suggested. Specifically, there is some evidence that a variation in the drifts around sunset may significantly contribute to the changes in the airglow pattern observed by TIMED-GUVI at latitudes close to the equatorial trough. It is likely that the same is true in the ionosphere, that some combination of the effects listed above result in the observed ionospheric density structure as several have been shown here to likely have sufficient strength to generate a change in the longitudinal structure of the F region ion densities.

[43] 5. The relative contribution of each of these effects to the $[O^+]$ in the TIME-GCM model, as well as thermosphere-ionosphere system remains to be determined. Such an investigation would require the use of better observational constraints for the amplitude and phase of each of the thermospheric and ionospheric parameters affected by atmospheric tides and a careful examination of the production,

loss and transport of O$^+$ associated with each wave component present in the TIME-GCM and observed.

[44] 6. By using the SAMI2 model, it has been possible to investigate the effects of the E and F region dynamos in isolation, but any investigation of the possible impacts of neutral zonal winds at F region altitudes or the feedback between changes to the ionospheric conductivity (such as may result from changing [O]/[N$_2$]) and the postsunset airglow is not possible with this model. The study of both of these effects, along with the contribution of individual tidal and planetary wave components is possible using the SAMI3 model and this will be the subject of a future work.

[45] **Acknowledgments.** This work was supported by the NASA Living With a Star program through the grant NNX07AT80G. The TIMED-GUVI analysis was supported by the NASA Heliophysics Guest Investigator program through the grant NNX07AG44G. J.D.H. was supported by ONR. The National Center for Atmospheric Research is sponsored by the National Science Foundation. The authors wish to thank Wenbin Wang for his comments on the initial draft of this paper.

[46] Zuyin Pu thanks the reviewers for their assistance in evaluating this paper.

References

Abdu, M. A., J. W. MacDougall, I. S. Batista, J. H. A. Sobral, and P. T. Jayachandran (2003), Equatorial evening prereversal electric field enhancement and sporadic E layer disruption: A manifestation of E and F region coupling, *J. Geophys. Res.*, *108*(A6), 1254, doi:10.1029/2002JA009285.

Appleton, E. V. (1946), Two anomalies in the ionosphere, *Nature*, *157*, 691, doi:10.1038/157691a0.

Burns, A. G., T. L. Killeen, G. R. Carignan, and R. G. Roble (1995), Large enhancements in the O/N$_2$ ratio in the evening sector of the winter hemisphere during geomagnetic storms, *J. Geophys. Res.*, *100*, 14,661–14,672, doi:10.1029/94JA03235.

Carruthers, G. R., and T. Page (1976), Apollo 16 far ultraviolet spectra of the terrestrial airglow, *J. Geophys. Res.*, *81*, 1683–1694, doi:10.1029/JA081i010p01683.

England, S. L., A. Dobbin, M. J. Harris, N. F. Arnold, and A. D. Aylward (2006a), A study into the effects of gravity wave activity on the diurnal tide and airglow emissions in the equatorial mesosphere and lower thermosphere using the Coupled Middle Atmosphere and Thermosphere (CMAT) general circulation model, *J. Atmos. Sol. Terr. Phys.*, *68*, 293–308, doi:10.1016/j.jastp.2005.05.006.

England, S. L., T. J. Immel, E. Sagawa, S. B. Henderson, M. E. Hagan, S. B. Mende, H. U. Frey, C. M. Swenson, and L. J. Paxton (2006b), Effect of atmospheric tides on the morphology of the quiet time, postsunset equatorial ionospheric anomaly, *J. Geophys. Res.*, *111*, A10S19, doi:10.1029/2006JA011795.

England, S. L., S. Maus, T. J. Immel, and S. B. Mende (2006c), Longitudinal variation of the E region electric fields caused by atmospheric tides, *Geophys. Res. Lett.*, *33*, L21105, doi:10.1029/2006GL027465.

England, S. L., T. J. Immel, and J. D. Huba (2008), Modeling the longitudinal variation in the postsunset far-ultraviolet OI airglow using the SAMI2 model, *J. Geophys. Res.*, *113*, A01309, doi:10.1029/2007JA012536.

England, S. L., Z. X., T. J. Immel, J. Forbes, and R. DeMajistre (2009), The effect of non-migrating tides on the morphology of the equatorial ionospheric anomaly: Seasonal variability, *Earth Planets Space*, *61*, 493–503.

Evans, D. (1987), Global statistical patterns of auroral phenomena, paper presented at Symposium on Quantitative Modeling of Magnetospheric-Ionospheric Coupling Processes, Kyoto Sangyo Univ., Kyoto, Japan.

Farley, D. T., E. Bonelli, B. G. Fejer, and M. F. Larsen (1986), The prereversal enhancement of the zonal electric field in the equatorial ionosphere, *J. Geophys. Res.*, *91*, 13,723–13,728, doi:10.1029/JA091iA12p13723.

Fejer, B. G., S. A. Gonzalez, E. R. de Paula, and R. F. Woodman (1991), Average vertical and zonal F region plasma drifts over Jicamarca, *J. Geophys. Res.*, *96*, 13,901–13,906.

Forbes, J. M., X. Zhang, S. Palo, J. Russell, C. J. Mertens, and M. Mlynczak (2008), Tidal variability in the ionospheric dynamo region, *J. Geophys. Res.*, *113*, A02310, doi:10.1029/2007JA012737.

Hagan, M. E., and J. M. Forbes (2002), Migrating and nonmigrating diurnal tides in the middle and upper atmosphere excited by tropospheric latent heat release, *J. Geophys. Res.*, *107*(D24), 4754, doi:10.1029/2001JD001236.

Hagan, M., and J. Forbes (2003), Migrating and nonmigrating semidiurnal tides in the upper atmosphere excited by tropospheric latent heat release, *J. Geophys. Res.*, *108*(A2), 1062, doi:10.1029/2002JA009466.

Hagan, M. E., A. Maute, R. G. Roble, A. D. Richmond, T. J. Immel, and S. L. England (2007), Connections between deep tropical clouds and the Earth's ionosphere, *Geophys. Res. Lett.*, *34*, L20109, doi:10.1029/2007GL030142.

Hagan, M. E., A. Maute, and R. G. Roble (2009), Tropospheric tidal effects on the middle and upper atmosphere, *J. Geophys. Res.*, *114*, A01302, doi:10.1029/2008JA013637.

Hanson, W. B., and R. J. Moffett (1966), Ionization transport effects in the equatorial F region, *J. Geophys. Res.*, *71*, 5559.

Hartman, W. A., and R. A. Heelis (2007), Longitudinal variations in the equatorial vertical drift in the topside ionosphere, *J. Geophys. Res.*, *112*, A03305, doi:10.1029/2006JA011773.

Häusler, K., H. Lühr, S. Rentz, and W. Köhler (2007), A statistical analysis of longitudinal dependences of upper thermospheric zonal winds at dip equator latitudes derived from CHAMP, *J. Atmos. Sol. Terr. Phys.*, *69*, 1419–1430, doi:10.1016/j.jastp.2007.04.004.

Häusler, K., H. Lühr, M. Hagan, A. Maute, and R. Roble (2010), Comparison of CHAMP and TIME-GCM nonmigrating tidal signals in the thermospheric zonal wind, *J. Geophys. Res.*, *115*, D00I08, doi:10.1029/2009JD012394.

Hedin, A. E. (1992), Horizontal wind model (HWM) (1990), *Planet. Space Sci.*, *40*, 556–557, doi:10.1016/0032-0633(92)90211-6.

Henderson, S. B., C. M. Swenson, A. B. Christensen, and L. J. Paxton (2005), Morphology of the equatorial anomaly and equatorial plasma bubbles using image subspace analysis of Global Ultraviolet Imager data, *J. Geophys. Res.*, *110*, A11306, doi:10.1029/2005JA011080.

Huba, J. D., G. Joyce, and J. A. Fedder (2000), Sami2 is Another Model of the Ionosphere (SAMI2): A new low-latitude ionosphere model, *J. Geophys. Res.*, *105*, 23,035–23,054, doi:10.1029/2000JA000035.

Immel, T. J., E. Sagawa, S. L. England, S. B. Henderson, M. E. Hagan, S. B. Mende, H. U. Frey, C. M. Swenson, and L. J. Paxton (2006), Control of equatorial ionospheric morphology by atmospheric tides, *Geophys. Res. Lett.*, *33*, L15108, doi:10.1029/2006GL026161.

Immel, T. J., S. L. England, Z. X. J. Forbes, and R. DeMajistre (2009), Upward propagating tidal effects across the E- and F-regions of the ionosphere, *Earth Planets Space*, *61*, 505–512.

Jin, H., Y. Miyoshi, H. Fujiwara, and H. Shinagawa (2008), Electrodynamics of the formation of ionospheric wave number 4 longitudinal structure, *J. Geophys. Res.*, *113*, A09307, doi:10.1029/2008JA013301.

Kato, S. (1956), Horizontal wind-systems in the ionospheric E region deduced from the dynamo theory of the geomagnetic S$_q$ variation. Part II. Rotating Earth, *J. Geomagn. Geolectr.*, *8*, 24–37.

Kato, S. (1957), Horizontal wind-systems in the ionospheric E region deduced from the dynamo theory of the geomagnetic S$_q$ variation. Part IV, *J. Geomagn. Geoelectr.*, *9*, 107–115.

Kil, H., S.-J. Oh, M. C. Kelley, L. J. Paxton, S. L. England, E. Talaat, K.-W. Min, and S.-Y. Su (2007), Longitudinal structure of the vertical E × B drift and ion density seen from ROCSAT-1, *Geophys. Res. Lett.*, *34*, L14110, doi:10.1029/2007GL030018.

Kil, H., E. R. Talaat, S.-J. Oh, L. J. Paxton, S. L. England, and S.-Y. Su (2008), Wave structures of the plasma density and vertical E × B drift in low-latitude F region, *J. Geophys. Res.*, *113*, A09312, doi:10.1029/2008JA013106.

Lin, C. H., C. C. Hsiao, J. Y. Liu, and C. H. Liu (2007), Longitudinal structure of the equatorial ionosphere: Time evolution of the four-peaked EIA structure, *J. Geophys. Res.*, *112*, A12305, doi:10.1029/2007JA012455.

Liu, H., and S. Watanabe (2008), Seasonal variation of the longitudinal structure of the equatorial ionosphere: Does it reflect tidal influences from below?, *J. Geophys. Res.*, *113*, A08315, doi:10.1029/2008JA013027.

Lühr, H., K. Häusler, and C. Stolle (2007), Longitudinal variation of F region electron density and thermospheric zonal wind caused by atmospheric tides, *Geophys. Res. Lett.*, *34*, L16102, doi:10.1029/2007GL030639.

Martyn, D. F. (1947), Atmospheric tides in the ionosphere. I. Solar tides in the F$_2$ region, *Proc. R. Soc. London, Ser. A*, *189*, 241–260.

Martyn, D. F. (1953), Electric currents in the ionosphere. III. Ionization drift due to winds and electric fields, *Philos. Trans. R. Soc. London, Ser. A*, *246*, 306–320.

Meléndez-Alvira, D. J., R. R. Meier, J. M. Picone, P. D. Feldman, and B. M. McLaughlin (1999), Analysis of the oxygen nightglow measured by the Hopkins Ultraviolet Telescope: Implications for ionospheric partial radiative recombination rate coefficients, *J. Geophys. Res.*, *104*, 14,901–14,914, doi:10.1029/1999JA900136.

Namba, S., and K.-I. Maeda (1939), *Radio Wave Propagation*, Corona, Toyko.

Oberheide, J., and J. M. Forbes (2008), Tidal propagation of deep tropical cloud signatures into the thermosphere from TIMED observations, *Geophys. Res. Lett.*, *35*, L04816, doi:10.1029/2007GL032397.

Pedatella, N. M., J. M. Forbes, and J. Oberheide (2008), Intra-annual variability of the low-latitude ionosphere due to nonmigrating tides, *Geophys. Res. Lett.*, *35*, L18104, doi:10.1029/2008GL035332.

Picone, J. M., A. E. Hedin, D. P. Drob, and A. C. Aikin (2002), NRLMSISE-00 empirical model of the atmosphere: Statistical comparisons and scientific issues, *J. Geophys. Res.*, *107*(A12), 1468, doi:10.1029/2002JA009430.

Rishbeth, H. (1971), The F-layer dynamo, *Planet. Space Sci.*, *19*, 263–267, doi:10.1016/0032-0633(71)90205-4.

Roble, R. (1995), Energetics of the mesosphere and thermosphere, in *The Upper Mesosphere and Lower Thermospere: A Review of Experiment and Theory*, *Geophys. Monogr. Ser.*, vol. 87, edited by R. Johnson and T. Killeen, pp. 1–21, AGU, Washington, D. C.

Roble, R. (1999), The NCAR thermosphere-ionosphere-mesosphere-electrodynamics general circulation model (TIME-GCM), in *STEP Handbook on Ionospheric Models*, edited by R. Schunk, pp. 281–288, Utah State Univ., Logan.

Roble, R. G., and E. C. Ridley (1994), A thermosphere-ionosphere-mesosphere-electrodynamics general circulation model (TIME-GCM): Equinox solar cycle minimum simulations (30–500 km), *Geophys. Res. Lett.*, *21*, 417–420, doi:10.1029/93GL03391.

Roble, R. G., and G. G. Shepherd (1997), An analysis of wind imaging interferometer observations of O(^{1}S) equatorial emission rates using the thermosphere-ionosphere-mesosphere-electrodynamics general circulation model, *J. Geophys. Res.*, *102*, 2467–2474, doi:10.1029/96JA02930.

Sagawa, E., T. J. Immel, H. U. Frey, and S. B. Mende (2005), Longitudinal structure of the equatorial anomaly in the nighttime ionosphere observed by IMAGE/FUV, *J. Geophys. Res.*, *110*, A11302, doi:10.1029/2004JA010848.

Scherliess, L., and B. G. Fejer (1999), Radar and satellite global equatorial F region vertical drift model, *J. Geophys. Res.*, *104*, 6829–6842, doi:10.1029/1999JA900025.

Scherliess, L., D. C. Thompson, and R. W. Schunk (2008), Longitudinal variability of low-latitude total electron content: Tidal influences, *J. Geophys. Res.*, *113*, A01311, doi:10.1029/2007JA012480.

Schunk, R., and A. Nagy (2000), *Ionospheres: Physics, Plasma Physics, and Chemistry*, pp. 324–327, Cambridge Univ. Press, Cambridge, U. K.

Thuillier, G., R. H. Wiens, G. G. Shepherd, and R. G. Roble (2002), Photochemistry and dynamics in thermospheric intertropical arcs measured by the WIND Imaging Interferometer on board UARS: A comparison with TIE-GCM simulations, *J. Atmos. Sol. Terr. Phys.*, *64*, 405–415, doi:10.1016/S1364-6826(01)00109-2.

Wan, W., L. Liu, X. Pi, M.-L. Zhang, B. Ning, J. Xiong, and F. Ding (2008), Wavenumber-4 patterns of the total electron content over the low latitude ionosphere, *Geophys. Res. Lett.*, *35*, L12104, doi:10.1029/2008GL033755.

Woodman, R. F. (1970), Vertical drift velocities and east-west electric fields at the magnetic equator, *J. Geophys. Res.*, *75*, 6249–6259, doi:10.1029/JA075i031p06249.

R. DeMajistre, Johns Hopkins University Applied Physics Laboratory, Laurel, MD 20723, USA.

S. L. England and T. J. Immel, Space Sciences Laboratory, University of California, Berkeley, CA 94720, USA. (england@ssl.berkeley.edu)

M. E. Hagan and A. Maute, High Altitude Observatory, National Center for Atmospheric Research, Boulder, CO 80307, USA.

J. D. Huba, Plasma Physics Division, Naval Research Laboratory, Washington, DC 20375, USA.